Supporting Information For

Local Electric Field in Nanocavities Dictates the Vibrational Relaxation Dynamics of Interfacial Molecules

Xiaoxuan Zheng[1], Quanbing Pei[1], Junjun Tan[2, *], Shiyu Bai[1], Yi Luo[1, 2, *], Shuji Ye[1, 2, *]

[1]*Hefei National Research Center for Physical Sciences at the Microscale, Department of Chemical Physics, University of Science and Technology of China, Hefei, Anhui, 230026, China*

[2]*Hefei National Laboratory, University of Science and Technology of China, Hefei, Anhui 230088, China*

*To whom all correspondence should be addressed.

Email: jjtan@ustc.edu.cn, yiluo@ustc.edu.cn, shujiye@ustc.edu.cn

Tel: 086-551-3603462

Table of Contents

1. Experimental sections

Preparation of the samples

The samples were prepared by the following method: first, a clean smooth gold film (a 10 nm thick Cr layer was evaporated onto a rotating silicon wafer, followed by a 100 nm thick Au layer) was soaked in the target molecular solution (10 mM, in ethanol) overnight to obtain a well-assembled SAM. The SAMs of thiophenol derivatives form ~1 nm thick spacer ($d \approx 1$ nm).[1-3] The sample was subsequently removed and washed with ethanol several times to eliminate physical adsorption. Without depositing gold nanoparticles, a sample without NPoMs (Au-SAMs) was formed. NPoMs were made by dispersing gold nanoparticles (Au NPs) on Au-SAMs. Au NPs with a diameter of approximately 55 nm are synthesized.[4] Then, the target molecules were covered with a layer of closely packed AuNPs using a Langmuir-Blodgett (LB) method,[5,6], and a relatively uniform and dense NPoM structure was formed. Figure S8 shows a scanning electron microscopy (SEM) image of the prepared sample, demonstrating the homogeneity of the substrate.

SFG-VS measurements

To avoid IR absorption by water vapor, we purged the light path chamber using dry air provided by the Orion air dryer (CRX 5J, Orion Machinery Co., Ltd, Dongguan, China) to maintain a relative humidity below 2%. All SFG experiments were carried out at room temperature (24°C). The SFG signals were generated by focusing the IR and visible beams on the sample surface with a focused spot diameter of ~ 200 μm. The incident angles for the IR and visible beams were 45° and 60°, respectively. The SFG

spectra of interfacial molecules with ppp (p-polarized SFG output, p-polarized visible input, and p-polarized infrared input) were collected. The SFG spectra were normalized by measuring the energy profile of the IR pulses determined by SFG signals from GaAs (110). The SFG signals were detected by an EMCCD camera (Newton 970 BVF, Andor) and dispersed into a spectrometer (Samrock 303i, Andor).

For the IR pump- SFG probe time-resolved SFG instrumentation, the incident angle of the pump IR was 53°. The pump IR was separated by an optical chopper to produce pump-on and pump-off SFG signals, which were split by a galvo mirror and imaged onto different rows of the CCD chip. A LABVIEW program was used to control the delay time between the pump IR pulse and the probe IR pulse. According to the ratio of the processed pump-on and pump-off spectra for the corresponding delay time, the population information of the ground state-excited state at a certain delay time is determined.

Fitting of the SFG-VS signal

The SFG signals were fitted using a standard procedure described in eq S1.[7]

$$I_{SFG} \propto \left| \chi_{NR}^{(2)} + \sum_{v} \frac{A_v}{\omega - \omega_v + i\Gamma_v} \right|^2 \quad \text{(S1)}$$

where $\chi_{NR}^{(2)}$ is the nonresonant background, and A_v, ω_v, and Γ_v are the strength, resonant frequency, and damping coefficient of the vibrational mode (v), respectively. $\chi_{NR}^{(2)}$ defaults to positive in the fitting. The peak frequency and bandwidth are used below as ω and Γ, respectively. The effective peak strength $\chi_v^{(2)}$ is defined as A_v/Γ_v. All the fitting parameters can be extracted by fitting the spectra.

2. The SE-SFG spectra of thiophenol derivatives

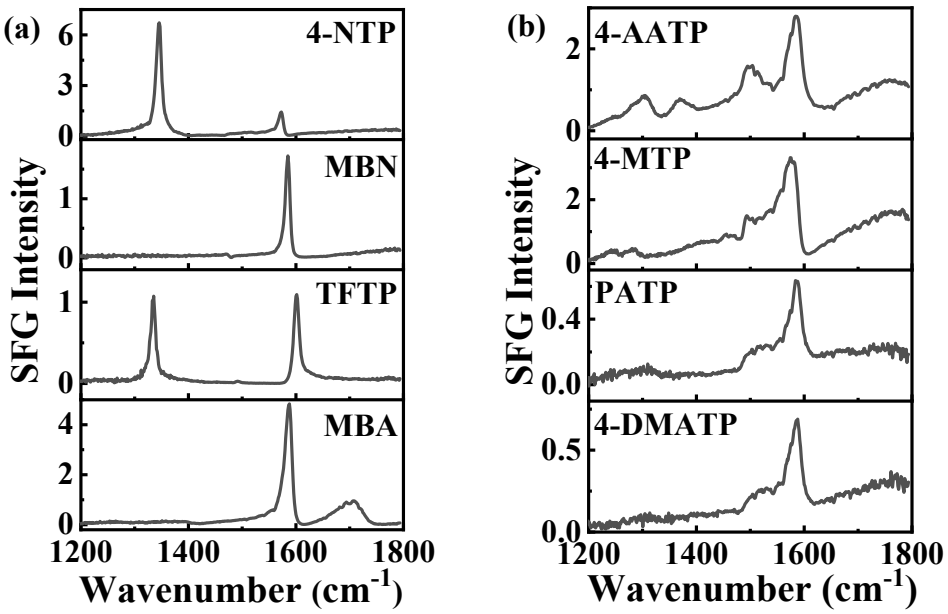

Figure S1. The SE-SFG spectra of thiophenol derivatives in the frequency range of 1200-1800 cm^{-1}

Figure S1 shows the ppp spectra of the NPoM-SAMs in the frequency range of of 1200-1800 cm^{-1}.

3. The SFG spectra of thiophenol derivatives

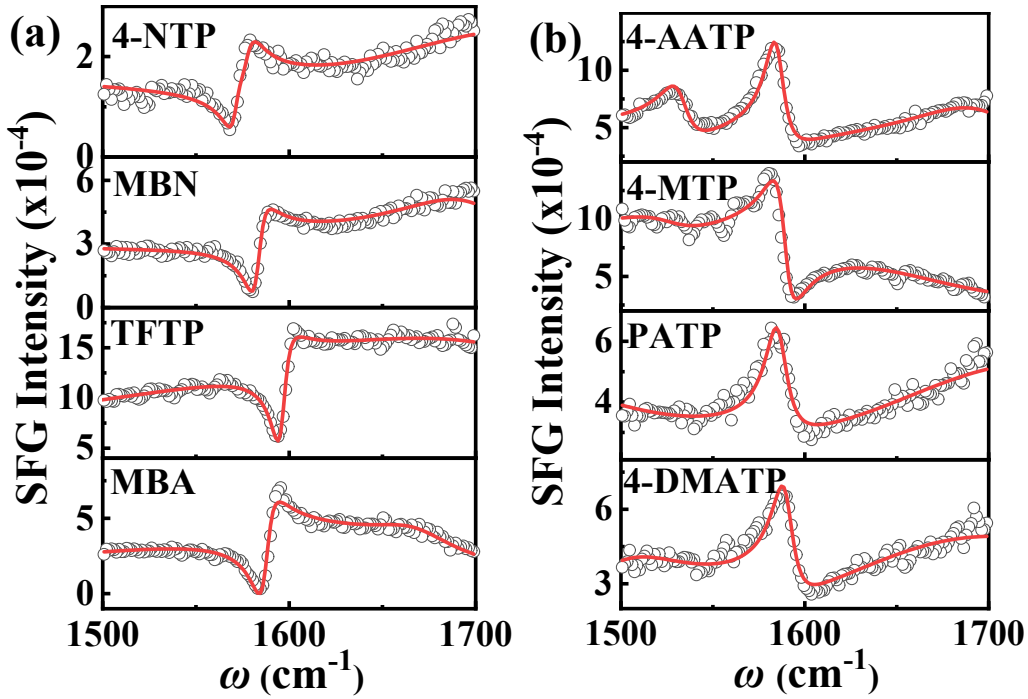

Figure S2. (a) The SFG spectra of 4-NTP, MBN, TFTP and MBA in the frequency

range of 1500-1700 cm^{-1}. (b) The SFG spectra of 4-AATP, 4-MTP, PATP and 4-DMATP in the frequency range of 1500-1700 cm^{-1}.

Figures S2a and S2b display the typical ppp spectra of the Au-SAM. The $\nu_{C=C}$ peaks in Figure S2a show a negative phase, indicating that the phase of the molecular resonance peak signal is opposite to the gold nonresonant signal.[8] In contrast, the $\nu_{C=C}$ peaks in Figure 1b exhibit a positive phase.

4. $\chi^{(2)}$ decay of the $\nu_{C=C}$ stretching vibration mode of the phenyl rings in the absence of NPoMs

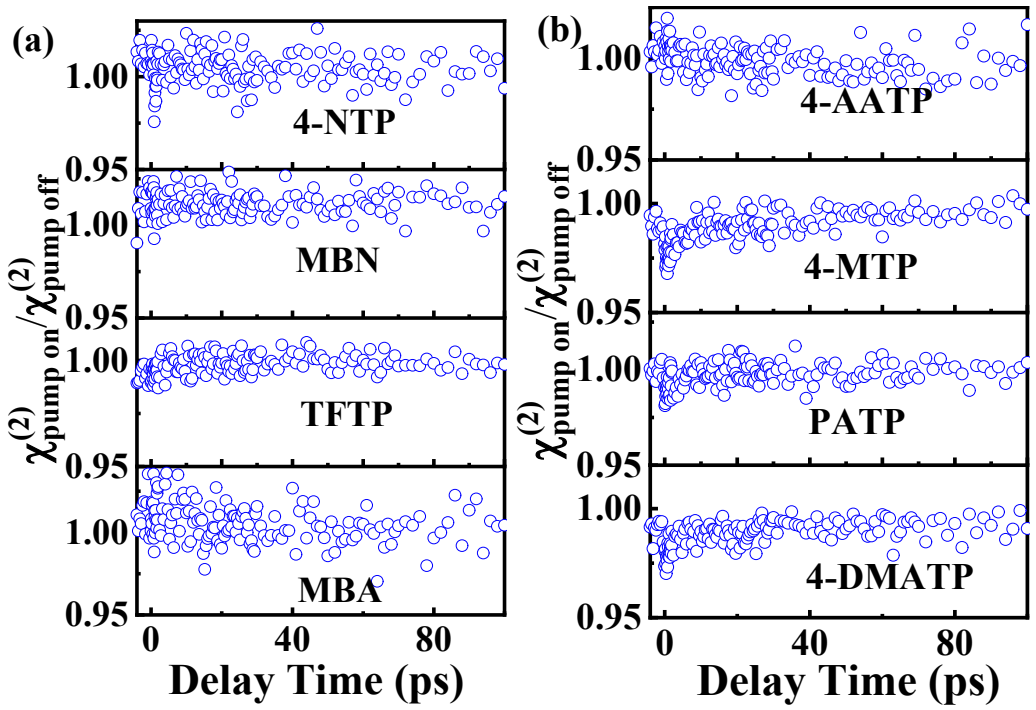

Figure S3. (a) $\chi^{(2)}$ decay of the $\nu_{C=C}$ mode of the phenyl rings of 4NTP, MBN, TFTP and MBA in the absence of NPoMs (b) $\chi^{(2)}$ decay of the $\nu_{C=C}$ mode of the phenyl rings of 4-AATP, 4-MTP, PATP and 4-DMATP in the absence of NPoMs.

Figure S3a and S3b display the $\chi^{(2)}$ decay of the $\nu_{C=C}$ of thiophenol derivatives in the absence of NPoMs. In the absence of nanocavities, the bleaching value is too small to be detected.

5. Potential-dependent SFG spectra of thiophenol derivatives

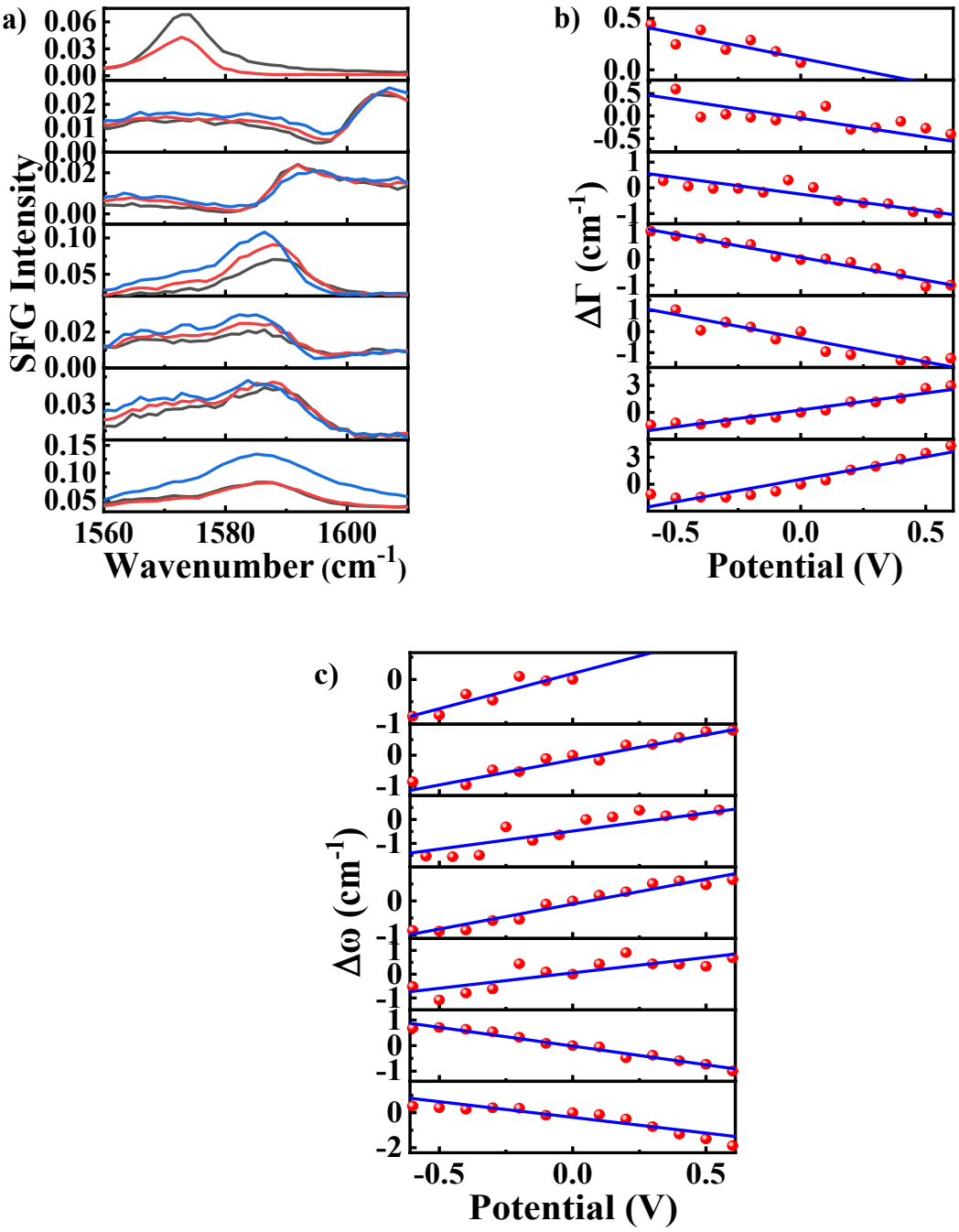

Figure S4. (a) Potential-dependent SFG spectra of thiophenol derivatives between 0.6 V and -0.6 V vs Ag/AgCl, black: -0.6 V, blue: 0.6 V, red:0 V. ΔΓ (b), Δω (c) of $\nu_{C=C}$ of thiophenol derivatives as a function of the electric field. The diagrams from top to bottom correspond to 4-NTP, TFTP, MBA, 4-AATP, 4-MTP, PATP, and 4-DMATP.

It should be noted that 4-NTP is damaged under positive potential; thus, only 0 V~-0.6 V data are used.

Note that the difference in the response of thiophenol derivatives to the electric field primarily arises from the modulation of the electronic properties of the phenyl ring by the substituents. However, the direction in the DC field has not been fully elucidated. Existing studies indicate that the ligand can alter the wavelength of the localized surface plasmon resonance (LSPR), whereby an EWG induces a blueshift in λ_{LSPR}, while an EDG leads to a redshift.[9] The excitation light with respect to the λ_{LSPR} determines the polarity of the electric field generated by the nanocavity. Indeed, recent investigations utilizing tip-enhanced Raman scattering (TERS) have revealed that variations in the coupling between the TERS tip and plasmonic structure can affect the sign of the DC electric field. In addition, the position of the TERS tip relative to the substructure can alter the sign of the DC electric field by affecting the hybrid tip-substrate plasmon resonance frequency.[10] In our study, we observed a close correlation between the sign of the electric field and σ. The direction of the electric field in our investigation varies with the substituent group, while the absolute value of the electric field is postulated to remain essentially constant.

6. Stark bandwidth broadening rate (k) as a function of the Hammett constant (σ)

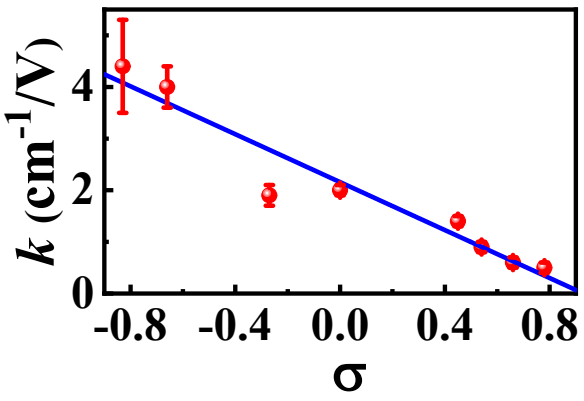

Figure S5. Stark bandwidth broadening rate (k) as a function of the Hammett constant (σ).

To more accurately obtain $k^{\sigma=0}$, we plot k against the σ of the para-substituted group on the phenyl ring and use the intercept as the value of $k^{\sigma=0}$, as shown in Figure S6. A good linear correlation between k and σ_R is observed, that is, k=(-2.3σ+2.2) cm^{-1}/V. Accordingly, we confirm that $k^{\sigma=0}$=2.2 cm^{-1}/V.

7. Determination of the magnitude of the electric field E_n using the Stark shift method

The magnitude of E_n can be further confirmed by the results determined using Stark shift (eqs. S2-S3), which is an acknowledged tool for quantifying electric fields.[11,12]

$$\mu^{\sigma} = \Delta\omega_p^{\sigma}/V \tag{S2}$$

$$E_n = \frac{\left(\omega_{NPoM}^{\sigma} - \omega_{Au}^{\sigma}\right)}{\mu^{\sigma}}/d \tag{S3}$$

where μ^{σ} is the Stark tuning coefficient and is given in cm^{-1}/V.[13] The dependence of the change in the $\nu_{C=C}$ peak shift ($\Delta\omega_p$) on V is shown in Figure 4c and S4c. The $\Delta\omega_p$ values of MBN, 4-NTP, TFTP, MBA, 4-AATP, and 4-MTP linearly increase (Figure 4c and

Figure S4c), while those of PATP and 4-DMATP linearly decrease (Figure S4c). The slope μ^{σ} is determined to be 1.5 (±0.4), 2.2 (±0.3), 1.5 (±0.3), 1.9 (±0.7), 1.2 (±0.2), 1.1 (±0.1), -1.4 (±0.2), and -2.6 (±0.6) cm^{-1}/V for 4-NTP, MBN, TFTP, MBA, 4-AATP, 4-MTP, PATP, and 4-DMATP, respectively (Table S6). The $\Delta\omega_n$ values measured in section 3.2 are -1.6, -2.3, -1.4, -2.2, -1.2, -1.2, -1.4, and -2.4 cm^{-1} for 4-NTP, MBN, TFTP, MBA, 4-AATP, 4-MTP, PATP, and 4-DMATP, respectively (Tables S4-5). The resulting magnitudes of E_n are deduced to be 1.1, 1.0, 0.9, 0.9, 1.0, 1.1, 1.0, and 0.9 V/nm for the corresponding samples.

8. Relaxation times of the thiophenol derivatives

Table S1. Relaxation times of the thiophenol derivatives.

thiophenol derivatives	A_1	T_1 (ps)	A_2	T_2 (ps)
4-NTP	-0.003 (±0.002)	0.6 (±0.4)	-0.1 (±0.03)	21.4 (±1.3)
MBN	-0.03 (±0.01)	1.1 (±0.3)	-0.1 (±0.04)	20.0 (±0.4)
TFTP	-0.06 (±0.02)	1.3 (±0.5)	-0.1 (±0.02)	17.3 (± 0.5)
MBA	-0.03 (±0.01)	0.7 (±0.3)	-0.2 (±0.03)	15.2 (±0.3)
4-AATP	-0.04 (±0.02)	0.8 (±0.4)	-0.2 (±0.04)	13.8 (±0.4)
4-MTP	-0.01 (±0.005)	0.3 (±0.1)	-0.2 (±0.05)	12.7 (±0.5)
PATP	-0.04 (±0.02)	0.9 (±0.5)	-0.1 (±0.04)	9.7 (±0.7)
4-DMATP	-0.03 (±0.01)	0.5 (±0.4)	-0.1 (±0.06)	10.4 (±1.4)

9. Fitting parameters for the ppp spectra shown in Figure S2(a-b) and Figure 1(a-b)

Table S2. Fitting parameters for the ppp spectra shown in Figure S2(a-b).

ppp		4-NTP	MBN	TFTP	MBA
	B_0	-0.02	0	-0.03	0
	$\chi_{NR}^{(2)}$	0.001	0.008	0.01	0.003
	A	-0.01	-0.01	-0.1	-0.02
Peak 1	ω (cm^{-1})	1572.0	1584.0	1597.2	1588.2
	Γ (cm^{-1})	4.0	4.8	5.0	5.2
	A	-0.01	0.07	0.05	0.02
Peak 2	ω (cm^{-1})	1577.7	1707.4	1485.8	1666.7
	Γ (cm^{-1})	5.5	43.5	12.4	26.2
ppp		4-AATP	4-MTP	PATP	4-DMATP
	B_0	-0.001	-0.01	-0.003	-0.01
	$\chi_{NR}^{(2)}$	0.003	0.001	0.002	0.02
	A	0.03	0.01	0.07	0.03
Peak 1	ω (cm^{-1})	1586	1587.7	1587.9	1588.7
	Γ (cm^{-1})	6.3	6.3	6.9	7.7
	A	0.02	0.003	0.03	0.01
Peak 2	ω (cm^{-1})	1533.5	1525.1	1529.3	1516.8
	Γ (cm^{-1})	9.0	23.8	11.3	14.8

Table S3. Fitting parameters for the ppp spectra shown in Figure 1(a-b).

ppp		4-NTP	MBN	TFTP	MBA
	B_0	-0.004	0	0	0

	$\chi_{NR}^{(2)}$	0.09	0	0	0.15
	A	1.0	0.8	0.4	2.6
Peak 1	ω (cm^{-1})	1570.0	1581.2	1596.2	1585.4
	Γ (cm^{-1})	4.6	5.0	5.3	6.7
ppp		4-AATP	4-MTP	PATP	4-DMATP
	B0	0	-0.02	-0.01	0.01
	$\chi_{NR}^{(2)}$	0	0.01	0.04	0.06
	A	0.8	0.5	1.8	1.5
Peak 1	ω (cm^{-1})	1586.2	1585.3	1585.5	1585.3
	Γ (cm^{-1})	8.5	8.4	11.4	11.6
	A	1.0			
Peak 2	ω (cm^{-1})	1528.8			
	Γ (cm^{-1})	23.3			

10. The averaging parameters for the ppp spectra of thiophenol molecules without and with nanocavities

Table S4. The averaging parameters for the ppp spectra of thiophenol molecules without nanocavities.

thiophenol derivatives	ω(cm^{-1})	Γ (cm^{-1})
4-NTP	1571.9 (±0.8)	4.1 (±0.4)
MBN	1584.0 (±1.6)	4.6 (±0.1)
TFTP	1597.1 (±1.8)	5.1 (±0.4)
MBA	1587.3 (±1.5)	5.3 (±0.4)

4-AATP	1587.3 (±1.7)	6.2 (±0.5)
4-MTP	1586.2 (±2.0)	6.3 (±0.7)
PATP	1588.0 (±1.6)	7.2 (±0.3)
4-DMATP	1588.7 (±2.6)	7.7 (±0.6)

Table S5. The averaging parameters for the ppp spectra of thiophenol molecules with nanocavities

thiophenol derivatives	ω(cm^{-1})	Γ (cm^{-1})
4-NTP	1570.3 (±1.3)	4.6 (±0.2)
MBN	1581.7 (±1.5)	5.2 (±0.1)
TFTP	1595.7 (±1.5)	5.8 (±0.2)
MBA	1585.5 (±1.4)	6.6 (±0.1)
4-AATP	1586.1 (±3.0)	8.2 (±0.4)
4-MTP	1585.0 (±0.5)	8.6 (±0.2)
PATP	1586.6 (±2.5)	11.2 (±0.3)
4-DMATP	1586.3 (±2.1)	12.1 (±0.5)

11. Stark tuning rates and Stark broadening rates of thiophenol derivatives

Table S6. Stark tuning rates and Stark broadening rates of thiophenol derivatives.

thiophenol derivatives	Stark tuning rates (cm^{-1}/V)	Stark broadening rates (cm^{-1}/V)
4-NTP	1.5 (±0.4)	-0.5 (±0.1)
MBN	2.2 (±0.3)	-0.6 (±0.1)

TFTP	1.5 (±0.3)	-0.9 (±0.1)
MBA	1.9 (±0.7)	-1.4 (±0.1)
4-AATP	1.2 (±0.2)	-2.0 (±0.1)
4-MTP	1.1 (±0.1)	-1.9 (±0.2)
PATP	-1.4 (±0.2)	4.0 (±0.4)
4-DMATP	-2.6 (±0.6)	4.4 (±0.9)

12. SEM image of the NPoMs and diagram of the cell used in the electrochemical experiments

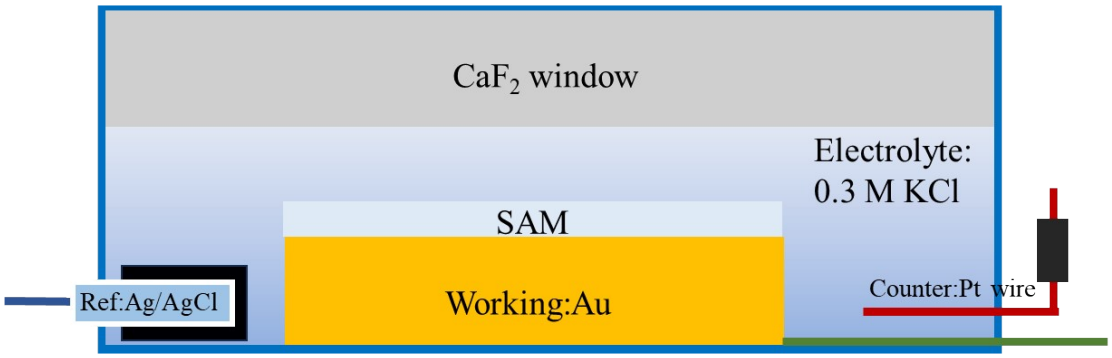

Figure S6. A diagram of the cell used in the electrochemical experiments.

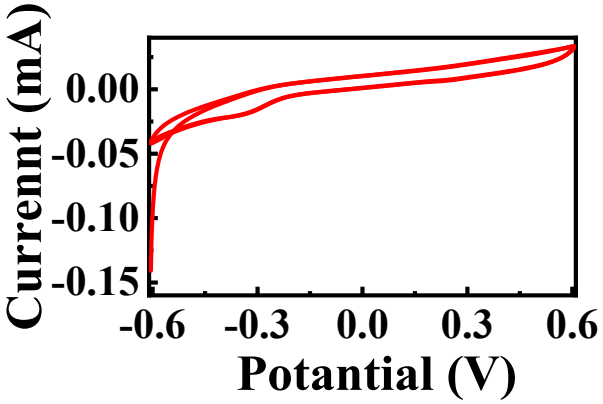

Figure S7. Representative cyclic voltammograms of thiophenol derivative monolayers.

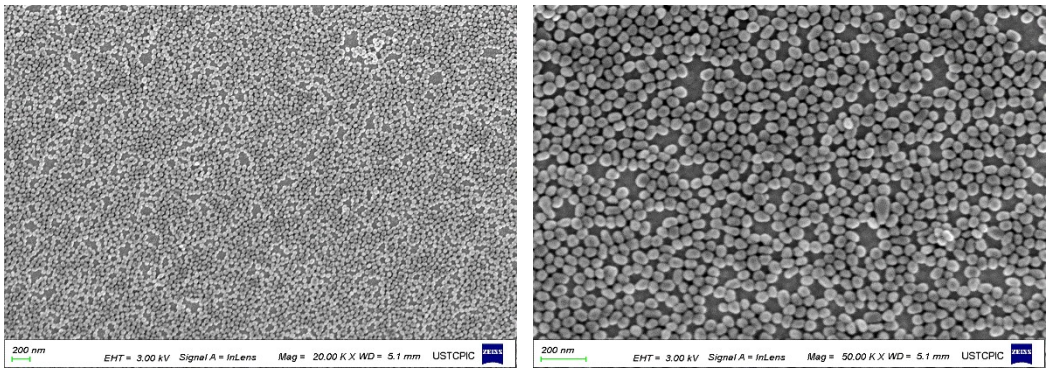

Figure S8. Scanning electron microscopy (SEM) image of the NPoMs.

References:

1 J. J. Baumberg, J. Aizpurua, M. H. Mikkelsen and D. R. Smith, Extreme Nanophotonics from Ultrathin Metallic Gaps, *Nat.Mater.,* 2019, **18**, 668-678.

2 H.-L. Wang, E.-M. You, R. Panneerselvam, S.-Y. Ding and Z.-Q. Tian, Advances of Surface-Enhanced Raman and Ir Spectroscopies: From Nano/Microstructures to Macro-Optical Design, *Light Sci. Appl.,* 2021, **10**, 161.

3 D. Wright, Q. Lin, D. Berta, T. Földes, A. Wagner, J. Griffiths, C. Readman, E. Rosta, E. Reisner and J. J. Baumberg, Mechanistic Study of an Immobilized Molecular Electrocatalyst by in Situ Gap-Plasmon-Assisted Spectro-Electrochemistry, *Nat. Catal.,* 2021, **4**, 157-163.

4 J. F. Li, X. D. Tian, S. B. Li, J. R. Anema, Z. L. Yang, Y. Ding, Y. F. Wu, Y. M. Zeng, Q. Z. Chen, B. Ren, Z. L. Wang and Z. Q. Tian, Surface Analysis Using Shell-Isolated Nanoparticle-Enhanced Raman Spectroscopy, *Nat. Protoc.,* 2013, **8**, 52-65.

5 H. Y. Jung, Y.-K. Park, S. Park and S. K. Kim, Surface Enhanced Raman Scattering from Layered Assemblies of Close-Packed Gold Nanoparticles, *Anal. Chim. Acta,* 2007, **602**, 236-243.

6 Y.-K. Park and S. Park, Directing Close-Packing of Midnanosized Gold Nanoparticles at a Water/Hexane Interface, *Chem. Mater.,* 2008, **20**, 2388-2393.

7 Y. R. Shen, *Principles of nonlinear optics*, Wiley-Interscience,New York, NY, USA, United States, 1984.

8 S. A. Sorenson, J. G. Patrow and J. M. Dawlaty, Solvation Reaction Field at the Interface Measured by Vibrational Sum Frequency Generation Spectroscopy, *J. Am. Chem. Soc.,* 2017, **139**, 2369-2378.

9 T. Liyanage, M. Nagaraju, M. Johnson, B. B. Muhoberac and R. Sardar, Reversible Tuning of the Plasmoelectric Effect in Noble Metal Nanostructures through Manipulation of Organic Ligand Energy Levels, *Nano Lett.,* 2020, **20**, 192-200.

10 M. T. Sheldon, J. van de Groep, A. M. Brown, A. Polman and H. A. Atwater, Plasmoelectric Potentials in Metal Nanostructures, *Science*, 2014, **346**, 828-831.

11 D. Bhattacharyya, P. E. Videla, M. Cattaneo, V. S. Batista, T. Lian and C. P. Kubiak, Vibrational Stark Shift Spectroscopy of Catalysts under the Influence of Electric Fields at Electrode-Solution Interfaces, *Chem. Sci.,* 2021, **12**, 10131-10149.

12 J. M. Marr and Z. D. Schultz, Imaging Electric Fields in SERS and TERS Using the Vibrational Stark Effect, *J. Phys. Chem. Lett.,* 2013, **4**, 3268-3272.

13 D. Wright, S. Sangtarash, N. S. Mueller, Q. Lin, H. Sadeghi and J. J. Baumberg, Vibrational Stark Effects: Ionic Influence on Local Fields, *J. Phys. Chem. Lett.,* 2022, **13**, 4905-4911.